

Discovery of Discrete Stages in the Oxidation of *exo*-Tetrahydrodicyclopentadiene (C₁₀H₁₆) Droplets Doped with Titanium–Aluminum–Boron Reactive Mixed-Metal Nanopowder

Ivan Antonov, Amandin Chyba, Sahan D. Perera, Andrew M. Turner, Michelle L. Pantoya, Matthew T. Finn, Albert Epshteyn, and Ralf I. Kaiser*



Cite This: *J. Phys. Chem. Lett.* 2022, 13, 9777–9785



Read Online

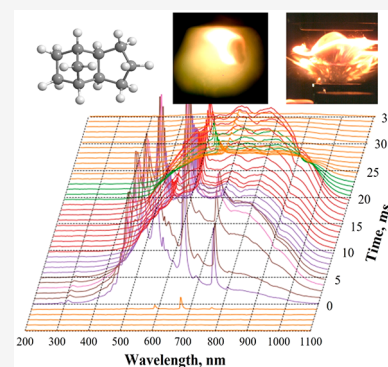
ACCESS |

Metrics & More

Article Recommendations

Supporting Information

ABSTRACT: Titanium (Ti), aluminum (Al), and boron (B) reactive mixed-metal nanopowders (Ti–Al–B RMNPs) represent attractive additives to hydrocarbon fuels such as *exo*-tetrahydrodicyclopentadiene (C₁₀H₁₆; JP-10) enhancing the limited volumetric energy densities of traditional hydrocarbons, but fundamental mechanisms and combustion stages in the oxidation have been obscure. This understanding is of vital significance in the development of next-generation propulsion systems and energy-generation technologies. Here, we expose distinct oxidation stages of single droplets of JP-10 doped with Ti–Al–B–RMNP exploiting innovative ultrasonic levitator technology coupled with time-resolved spectroscopic (UV–vis) and imaging diagnostics (optical and infrared). Two spatially and temporally distinct stages of combustion define a glow flame stage in which JP-10 and nanoparticles combust via a homogeneous gas phase (Al) and heterogeneous gas-surface oxidation (Ti, B) and a slower diffusion flame stage associated with the oxidation of JP-10. These findings enable the development of next-generation RMNP fuel additives with superior payload delivery capabilities.



Since the first isolation of elemental boron as a reduction product of boric acid with potassium by Humphry Davy more than 200 years ago,¹ boron-based nanostructures have captivated the attention of the computational,² inorganic,³ medicinal,⁴ and physical chemistry communities⁵ from the fundamental viewpoints of electronic structure theory⁶ and chemical bonding⁷ along with applications in cancer treatment (neutron capture therapy),⁸ material sciences (borophenes,⁹ fullerene-type boron cages¹⁰), and high-energy-density materials.^{11,12} With a volumetric energy density of 138 kJ cm⁻³, particular attention has been devoted to the synthesis of boron nanoparticles^{11,13,14} as additives to hydrocarbon fuels such as *exo*-tetrahydrodicyclopentadiene (C₁₀H₁₆, JP-10) in air-breathing propulsion systems.^{13,15} These nanoparticles exceed the limited volumetric energy densities of traditional hydrocarbons (35–40 kJ cm⁻³) and of combustible metals such as aluminum (84 kJ cm⁻³). However, the exploitation of boron in combustion systems revealed vital limitations such as the creation of an inert layer of boron oxide (B₂O₃) on the surface¹⁶ and the formation of gaseous metaboric acid (HOBO), resulting in ignition delays and inhibiting a complete oxidation and hence full energy release.¹⁷

Reactive mixed-metal nanopowders (RMNPs) containing titanium (Ti), aluminum (Al), and boron (B), where the metals are combined using wet chemical techniques with molecular metal hydride precursors and produce materials where the reactive metals are mixed at the atomic level, represent an

attractive alternative to mitigate these long-standing obstacles.^{15,18,19} The addition of titanium and aluminum has been implicated in the initiation of exoergic reactions with boron, forming borides along with heating of the RMNPs to a temperature of 2130 K, at which boron oxidation occurs, thus eliminating oxide layers and relieving the problem of the kinetic trapping of boron as metaboric acid.²⁰ Benchmark studies exploiting Ti–Al–B RMNPs suspended in hydrocarbon fuels resulted in shorter ignition delays and increased burn durations.^{20–22} However, although Ti–Al–B RMNPs are a promising class of high-energy-density fuel additives with volumetric energy contents of up to 92 kJ cm⁻³,^{19,20} there is a critical lack of knowledge of the fundamental elementary mechanisms and of distinct combustion stages involved in the oxidation of hydrocarbon fuel such as JP-10 in the presence of metal-based nanoparticles. This understanding is of vital importance in the development of next-generation propulsion systems along with energy-generation technologies and requires the identification of key reaction intermediates along with the

Received: August 26, 2022

Accepted: September 23, 2022

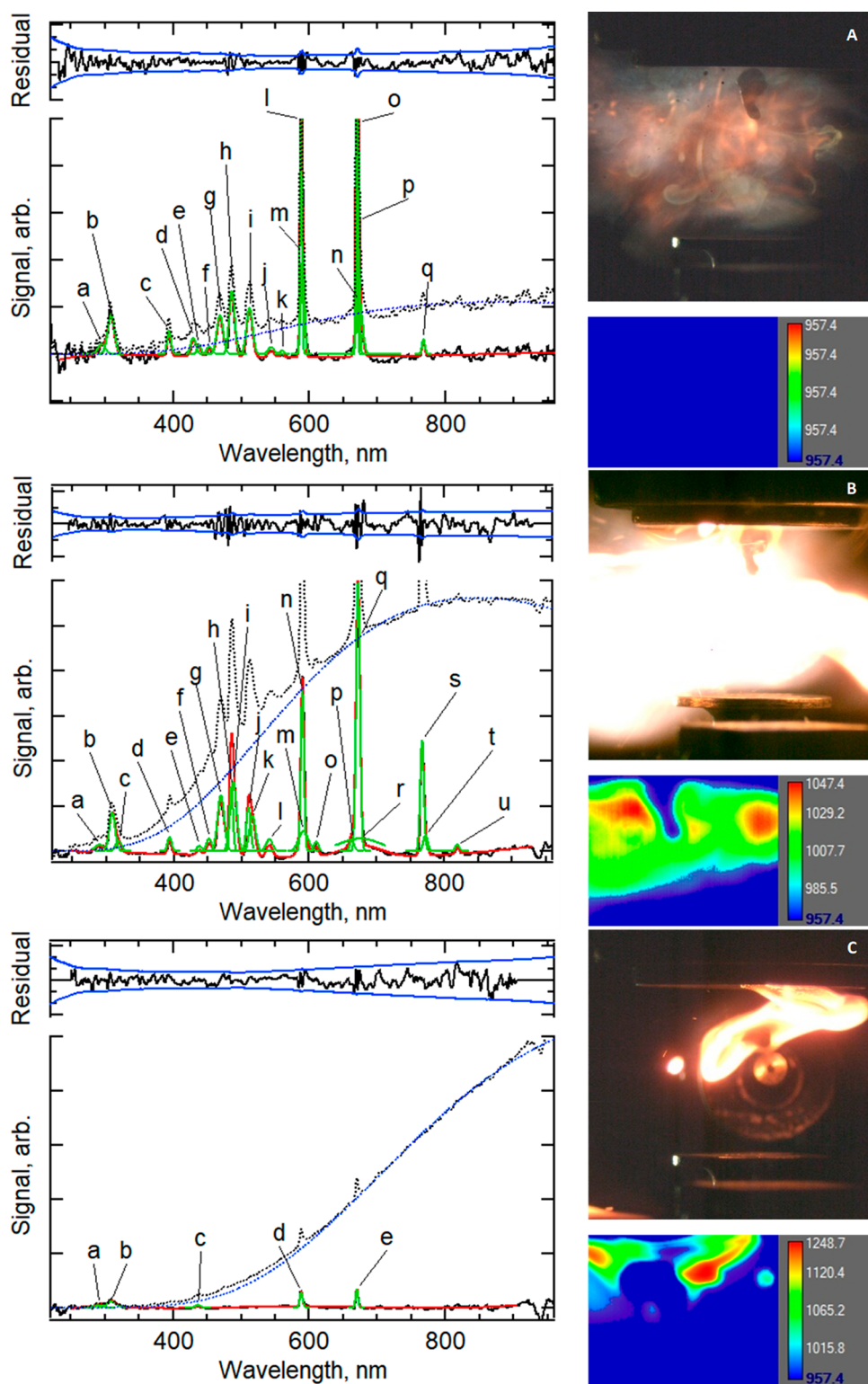


Figure 1. Background-corrected UV–vis emission spectrum (left panel) of the combustion of JP10-AINPs, with optical and infrared images (top and bottom right panels) of the ignition of JP10-AINPs recorded at $t = 0$ ms (A), 4 ms (B), and 17 ms (C) after ignition. The black dotted line is the emission spectrum, and the blue dotted line is the blackbody radiation background. The black solid line is the background-corrected emission spectrum, and the red and green solid lines are the total and individual peak fits, respectively. The fit residual (black solid line) is overlaid with a $\pm 2\sigma$ uncertainty interval (blue solid lines). Temperatures are given in degrees Celsius. Assignments of the deconvoluted emissions are compiled in Tables S3–S5.

products and the time-resolved oxidation sequence of the metal nanoparticle components (Ti, Al, and B) together with the hydrocarbon fuel.

Here, we report on the very first *in situ* detection of distinct oxidation stages of single droplets of JP-10,²³ a high-energy-density, bicyclic hydrocarbon doped with a titanium–alumi-

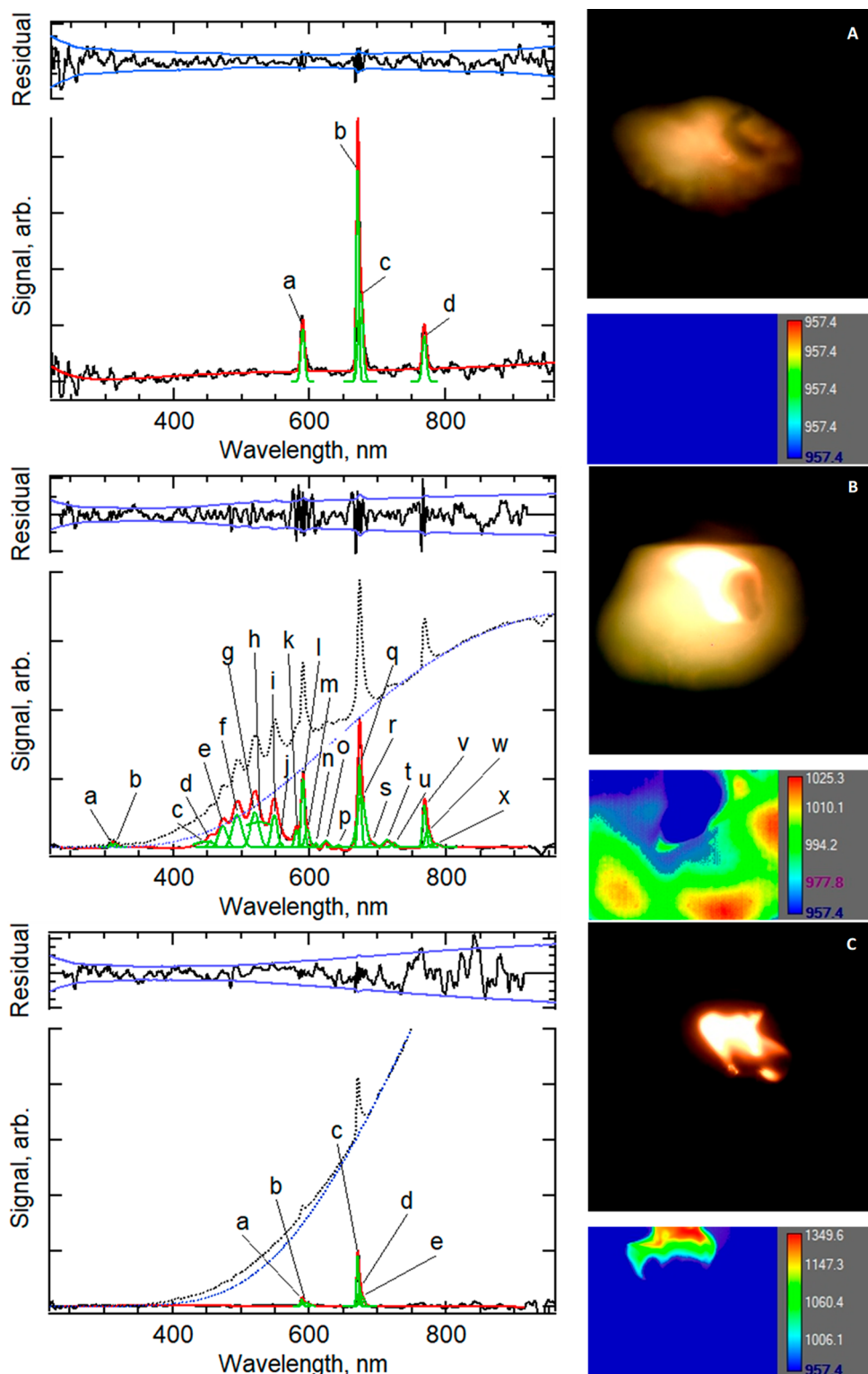


Figure 2. Background-corrected UV–vis emission spectrum (left panel) of the combustion of JP10–TiAlB RMNPs, with optical and infrared images (top and bottom right panels) of the ignition of JP10–TiAlB RMNPs recorded at $t = 0$ ms (A), 2 ms (B), and 29 ms (C) after ignition. The black dotted line is the emission spectrum, and the blue dotted line is the blackbody radiation background. The black solid line is the background-corrected emission spectrum, and the red and green solid lines are the total and individual peak fits, respectively. The fit residual (black solid line) is overlaid with a $\pm 2\sigma$ uncertainty interval (blue solid lines). Temperatures are given in degrees Celsius. Assignments of the deconvoluted emissions are compiled in Tables S6–S8.

num–boron reactive mixed-metal nanopowder (Ti–Al–B RMNP). This has been achieved through innovative time-resolved oxidation studies of the droplets exploiting an

ultrasonic levitator coupled with a complementary array of time-resolved spectroscopic detection techniques and imaging diagnostics (Supporting Information Figures S1–S4). Ultra-

sonic levitation has the unique advantage of exploring the oxidation of single droplets of metal-doped organic fuel under containerless conditions, thus eliminating interfering wall effects.^{20,24–26} The ignition of each droplet is triggered by a carbon dioxide laser pulse in an argon–oxygen atmosphere, and the oxidation is traced by synchronized thermal imaging and high-speed optical cameras along with time-resolved ultraviolet–visible (UV–vis) emission spectroscopy. This strategy not only allows the recording of the time-resolved emission spectra of well-defined combustion species, rather than averaging over the complete combustion process,^{20,24,26} but also characterizes previously uncharted, distinct oxidation stages in Ti–Al–B RMNP-doped fuel droplets involving two spatially and temporally distinct stages of combustion as achieved through a novel, automated analysis of the ultraviolet–visible emission spectra.

These stages include a glow flame stage in which small droplets of fluid spray quickly combust and a much slower diffusion flame stage of combustion associated with the hydrocarbon fluid in larger droplets. Chemically, the first glow flame stage is associated with the combustion of the hydrocarbon and the nanoparticles. Aluminum oxide (AlO) is formed through gas-phase reactions of atomic aluminum with molecular oxygen, whereas heterogeneous chemistry accounts for the generation of titanium oxide (TiO), boron monoxide (BO), and boron dioxide (BO₂). Molecules are formed in the combustion process of the hydrocarbon fuel (C₂, OH, and CH) and of the nanoparticles (BO, AlO, TiO, and BO₂) as identified through tracing their emission features over time. The second diffusion flame stage is associated with principally hydrocarbon combustion. Hence, the fundamental difference between these stages is the nonparticipation of the nanoparticles in the combustion during the second stage, while nanoparticles are oxidized in the first stage via homogeneous gas-phase (Al) and heterogeneous gas-surface chemistry (Ti and B). These findings have a profound impact on the design of nanoparticle-doped hydrocarbon fuels involving Ti–Al–B RMNPs as a benchmark ultimately enabling the development of next-generation fuel additives and air-breathing transportation systems with superior performance and payload delivery capabilities.

An elucidation of distinct combustion and temperature regimes during the oxidation of JP-10 droplets in the presence of Ti–Al–B RMNPs requires a comparison of a reference system containing nanoparticles of a single metal only. This is accomplished here for the oxidation of JP-10 droplets doped with aluminum nanoparticles (AlNPs) as a baseline. Typically, the overall combustion process of a single droplet occurs in less than 1 s. Nonetheless, soon after ignition, all systems exhibit resonance instabilities due to variations of the gas temperature and composition in the flame region, which affect the speed of sound and therefore the resonance conditions of the supersonic levitator. This results in droplets plunging out of the trap after 30–50 ms of burning.

The synchronized emission spectra and optical and infrared (IR) images of the combustion for the JP-10/AlNPs and JP-10/Ti–Al–B RMNPs systems are visualized in Tables S1 and S2. Selected representative emission spectra along with optical and infrared images corresponding to ignition as well as early and late combustion are shown in Figures 1 (AlNPs) and 2 (Ti–Al–B RMNPs). Prior to ignition, exposure by the carbon dioxide laser results in the formation of a cloud of white fog which expands in a 1 to 3 cm³ volume around the droplet (Table S1 and Movies S1 and S2). The white color of the fog is produced by

Mie scattering of the illuminating light-emitting diode (LED) light, hence the fog consists of nanofluid droplets that are comparable to or larger than the wavelengths of visible light (400 to 700 nm). Occasionally, the ignition of individual metal particles is detected as bright sparks traveling through the camera field of view at high velocities. The start of droplet ignition is determined by the first video frame that exhibits a rapidly growing flame envelope. The time of ignition (Figures 1A and 2A) is referenced as time zero (0 ms). Following the ignition, the flame quickly expands through the nanofluid spray cloud, and after 2–4 ms, it reaches its maximum size and brightness (Figures 1B and 2B). Several milliseconds later, the flame intensity subsides (Tables S1 and S2), and its internal structure becomes visible in the form of bright plumes attached to darker spheroid regions and a glow that surrounds the plumes. The plumes and the spheroid regions represent a diffusion flame attached to macroscopic (millimeter-sized) JP-10 droplets. The glow is produced by the combustion of the JP-10 vapors and the nanofluid spray. After 10 to 15 ms, the glow flame disappears and only the diffusion flame plumes remain (Figures 1C and 2C).

The IR camera complements the optical video by providing measurements of the flame temperature. The temperature measured by the IR camera is proportional to the flame emissivity ϵ , which shows significant spatial and temporal changes during droplet combustion. For flame sizes observed in this work, ϵ is less than 1; therefore, the IR camera underestimates the flame temperature by a factor of 2 to 3.^{20,26} The flame emissivity ϵ becomes sufficiently high for the detection by the IR camera operating at a combustion-relevant temperature range after 2 to 3 ms. The highest temperatures of about 1500 K, as measured by the IR camera, are seen in the diffusion flame plumes attached to burning macroscopic droplets at later times whereas the glow flame at early times has temperatures of 900 to 1100 K. The high emissivity of these flames is determined by the presence of efficient broadband emitters such as soot and hot nanoparticles. Representative time profiles of temperature and radiated power for the JP-10-AlNPs and JP-10–Ti–Al–B RMNP systems extracted from the emission spectra (Supporting Information) are presented in Figure 3. A comparison of the AlNP and the Ti–Al–B RMNP systems discloses stimulating discoveries. For both systems, after ignition at time zero, a sharp temperature rise (dT/dt_{\max}) of dT/dt_{\max} larger than $2 \times 10^6 \text{ K s}^{-1}$ is observed. The temperature, as measured by the emission spectra, quickly reaches peak values at 2800 to 3000 K. After a quick initial rise, it decreases to the 2000 K range in 20 ms. While the postignition temperature profiles show relatively small variations, both systems demonstrate temporal oscillations of the radiated power. The AlNP system reaches its peak power 3 ms after ignition, followed by a quick decay to baseline values. Ti–Al–B RMNPs show more complex behavior where the radiated power peaks first at 5 ms and then after a short plateau increases again near 18 ms to a higher peak. The early maximum of the blackbody radiation correlates in time with the maximum intensity of the glow region produced by burning of the nanofluid spray (Figure 3, Table S2) and can be attributed to the emission of airborne nanoparticles. The second maximum correlates in time with the formation of a plume attached to a liquid droplet and therefore can be connected to the soot produced in the fuel-rich flame near a liquid JP-10 surface. AlNP data did not show the second maximum because the JP-10 droplet in this particular experiment was temporarily brought to the upper node of the levitator and left the field of view of the emission probe.

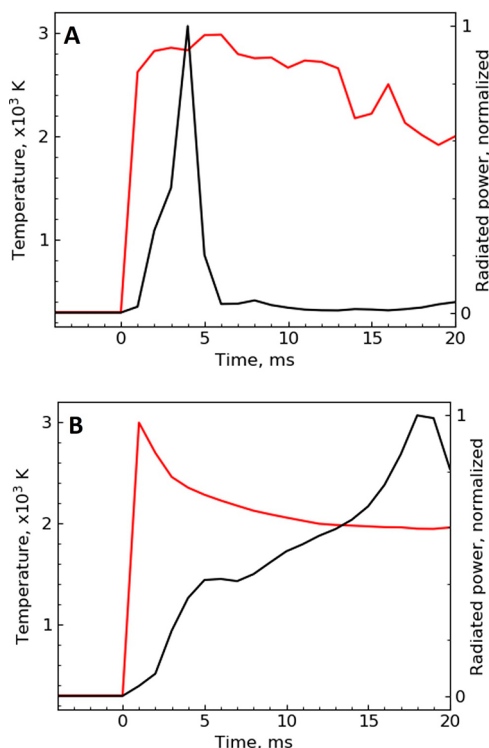


Figure 3. Temperature (red trace) and total radiated power (black trace) time profiles for the combustion of JP10-AINP (A) and JP10-TiAlB RMNP (B) droplets derived from the blackbody emission radiation. Temperature 1σ error bars (not shown) are below ± 10 K.

For the JP-10-AINPs and JP-10-Ti-Al-B RMNP systems, UV-vis emission spectra were collected, time-resolved over 127 ms with data collection times of 1 ms per spectrum (Figure 4), and synchronized with the optical and visual cameras (Figures S3 and S4). In both systems, the stages of glow and diffusion flame result in qualitatively different emission spectra. The glow flame at $t = 0$ –15 ms has multiple atomic and molecular emission peaks superimposed on a blackbody background spectrum. The diffusion flame at $t > 15$ ms is dominated by very strong blackbody broadband emission and reveals few weak emission peaks that change in intensity as the burning droplet moves in and out of the field of view of the emission probe. Representative blackbody-corrected deconvoluted UV-vis emission spectra of the JP-10-AINPs and JP-10-Ti-Al-B RMNP flames recorded at ignition, during glow flame and diffusion flame stages, are displayed in Figures 1 and 2, respectively, while the extracted temporal evolutions of the emission features during the glow stage are compiled in Figure 5.

The oxidation of aluminum is associated with the emission lines of aluminum at 395 nm (Al; $2p^63s^24s^2S \rightarrow 2p^63s^23p^2P$) and aluminum monoxide at 460–550 nm (AlO; $B^2\Sigma^+ \rightarrow X^2\Sigma^+$) (Figure 1). While the oscillator strength is higher for the Al atomic line, its emission is much less intense than that of the AlO bands. This suggests that Al atoms are quickly removed in reactions with molecular oxygen and JP-10 vapor in a barrierless, exoergic reaction (-15 kJ mol $^{-1}$). The time behavior of Al and AlO emissions (Figure 5A) is characterized by a quick rise to peak values at 2 ms followed by a decay to the baseline at 8–10 ms. Thus, the time traces of atomic aluminum (Al) and aluminum oxide (AlO) correlate with the glow flame produced by burning of the AINPs in the nanofluid spray. The simultaneous presence of Al and AlO in the gas phase is

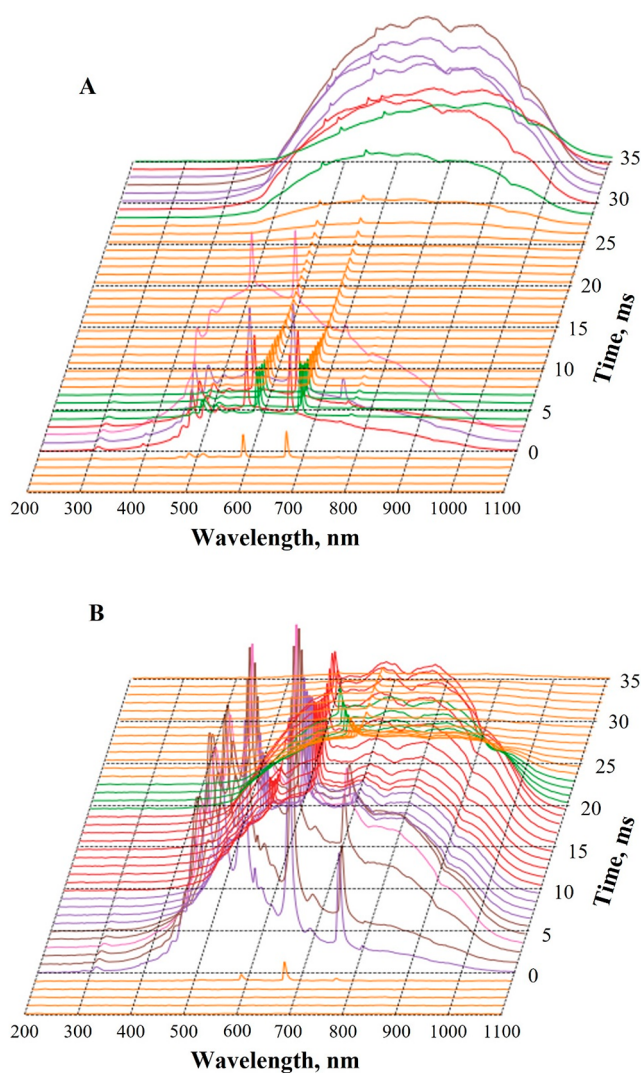


Figure 4. UV-vis emission spectra in steps of 1 ms collected during 40 ms of the ignition of JP10-AINP (A) and JP10-TiAlB RMNP (B) droplets.

consistent with a computationally suggested mechanism of AINP combustion, where AlO is formed in the gas phase through the reaction of aluminum atoms with molecular oxygen.²⁷ The fast rise of Al and AlO concentrations is produced by the quick heating of NPs to temperatures of about 3000 K above the melting point of aluminum oxide (Al₂O₃, 2345 K)^{26,28} and to produce Al vapor close to the boiling point of Al (2743 K). The decay of the Al and AlO time traces can be explained by lowering the Al vapor pressure due to the reduction of temperature and the total surface area of the NPs upon oxidation.

The most prominent emission features in the combustion of JP-10-AINPs are atomic lines of sodium, lithium, and potassium at 589 nm (Na: $2p^63p^2P \rightarrow 2p^63s^2S$), 672 nm (Li: $1s^22p^2P \rightarrow 1s^22s^2S$), and 767 nm (K: $3p^64p^2P \rightarrow 3p^64s^2S$), respectively (Figure 1, Tables S3–S5). The alkali metals represent trace elements in the nanoparticles.^{26,28} Their time traces show a sharp rise at 2 ms followed by a slower decline to the baseline level over the subsequent 20 ms (Figure 5A), qualitatively similar to the Al and AlO species. This suggests that the major source of alkali metals is evaporation from the NPs. Thus, the rise of Na, Li, and K can be produced by quick heating of the NPs

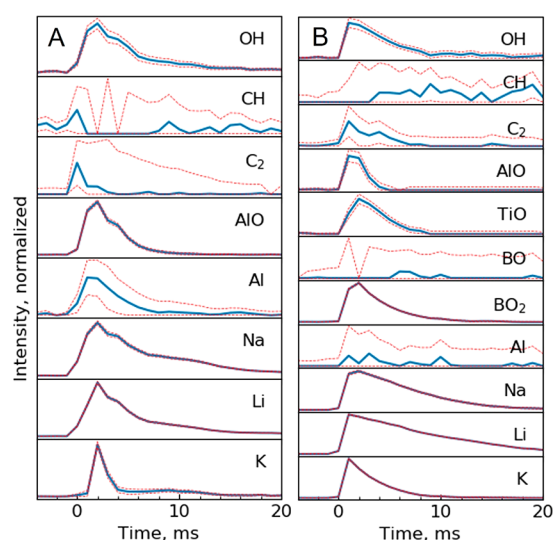


Figure 5. (A) Temporal profiles of hydroxyl (OH), methylidene (CH), dicarbon (C_2), aluminum monoxide (AlO), aluminum (Al), sodium (Na), lithium (Li), and potassium (K) atoms in JP10-AINP droplet combustion. (B) Temporal profiles of hydroxyl (OH), methylidene (CH), dicarbon (C_2), aluminum monoxide (AlO), titanium monoxide (TiO), boron monoxide (BO), boron dioxide (BO_2), aluminum (Al), sodium (Na), lithium (Li), and potassium (K) atoms in JP10-TiAlB RMNP droplet combustion. Blue solid traces are time profiles, and red dashed traces are 1σ error bounds. All temporal profiles were generated by the constrained linear least-squares procedure as defined in the Supporting Information.

to peak temperatures at early times, whereas the decay can be explained by the reduction of the NP temperature and surface area upon oxidation. Also evident in the emission spectra are dicarbon (C_2 ; $d^3\Pi_g^- \rightarrow a^3\Pi_u$), hydroxyl (OH; $A^2\Sigma^+ \rightarrow X^2\Pi$), and methylidyne (CH; $A^2\Delta \rightarrow X^2\Pi$) peaks, which are linked to the oxidation of JP-10. The emission of C_2 and CH is greatest at 1 ms and reduces to baseline levels at 2–4 ms. The early rise of CH and C_2 emission suggests that the oxidation of JP-10 precedes oxidation of the AINPs in the nanofluid spray and serves as a heating mechanism for the latter. The hydroxyl emission time trace is similar to the Al-containing species: it peaks at 2 ms and slowly decays to the baseline after 15 ms. The slower rise and decay of the OH emission compared to the CH and C_2 emission can be explained by a population of OH radicals being produced in the reaction of AlO molecules with water vapor.^{27,29} When the glow flame is extinguished, the emission spectrum of the diffusion flame (Figure 1C) is dominated by the broadband blackbody radiation and shows relatively weak emission features of hydroxyl (OH), dicarbon (C_2), sodium (Na), and lithium (Li) atoms (Figure 1C). The absence of AINP oxidation products in the diffusion flame suggests that it is produced solely by the JP-10 oxidation. The weak atomic Na and Li emissions at this stage can be explained by small amount of the trace alkali metals being extracted into JP-10 after the preparation of the nanofluid.

The emission spectra of the JP-10/Ti–Al–B RMNPs system are more complex compared to those of the JP-10/AINPs system (Figure 2). Considering the elemental composition of the Ti–Al–B RMNPs, moderately strong emissions of aluminum monoxide (AlO; $B^2\Sigma^+ \rightarrow X^2\Sigma^+$) at 460–520 nm and titanium monoxide (TiO; $A^3\Phi \rightarrow X^3\Delta$) at 714 nm are visible. Boron combustion is represented by weak bands of boron monoxide (BO; $A^2\Pi \rightarrow X^2\Sigma^+$) and dominant $A^2\Pi_u^- \rightarrow$

$X^2\Pi_g$ emission bands of boron dioxide (BO_2). The time behavior of BO_2 and TiO time traces is characterized by a quick rise to peak values at 2 ms followed by a decay to the baseline at 8–10 ms. AlO peaks earlier at 1 ms and shows a faster decay to the baseline at 4 ms. Also visible are weak lines of atomic aluminum at 395 nm (Al; $2p^63s^24s^2S \rightarrow 2p^63s^23p^2P$); however, no atomic emissions of boron or titanium were observed. Titanium and boron boil at 3560 and 4273 K, respectively, so only Al, which boils at 2743 K, evaporates at the observed temperatures. Thus, TiO, BO, and BO_2 must be produced in surface reactions of RMNPs with molecular oxygen and emitted into the gas phase, whereas aluminum monoxide can be produced in the gas-phase oxidation of Al atoms. Therefore, the comparatively faster decay of AlO emission after 4 ms can be explained by the simultaneous cooling of the system to below the boiling temperature of aluminum (Figure 3B). Strong atomic emissions of trace alkali metals are present for atomic lithium, sodium, and potassium at 672 nm (Li: $1s^22p^2P \rightarrow 1s^22s^2S$), 589 nm (Na: $2p^63p^2P \rightarrow 2p^63s^2S$), and 767 nm (K: $3p^64p^2P \rightarrow 3p^64s^2S$), respectively (Figure 2). These impurities were observed in previous studies;^{20–22} in particular, Li may originate from lithium aluminum hydride ($LiAlH_4$) and lithium borohydride ($LiBH_4$) used for the preparation of the Ti–Al–B RMNPs. The alkali atom emissions peak at $t = 1$ to 2 ms, followed by a slow decay to the baseline at 12–18 ms, similar to their behavior in AINPs. As in the AINPs, the source of Na, Li, and K is outgassing from the Ti–Al–B RMNPs at elevated temperatures. Emission lines resulting from the oxidation of JP-10 are prominent for dicarbon (C_2 ; $d^3\Pi_g^- \rightarrow a^3\Pi_u$), methylidyne (CH; $A^2\Delta \rightarrow X^2\Pi$ and $B^2\Sigma^- \rightarrow X^2\Pi$), and hydroxyl radicals (OH; $A^2\Sigma^+ \rightarrow X^2\Pi$). CH and C_2 bands are weak and quickly overwhelmed by much stronger BO_2 emissions. On the other hand, the OH band at 308 nm is very strong and shows a quick rise at 1 ms followed by a slow decay to the baseline at 8 ms, which is qualitatively similar to the time traces of alkali metals and the metal oxides BO_2 and TiO. In parallel with AINPs, the slow decay of the OH time trace can be explained if OH radicals are produced in the NPs chemistry, e.g., in reactions of gaseous BO_2 with H_2O ³⁰ or in surface reactions of absorbed water with boron oxides.^{17,31} In the diffusion flame stage, the emission spectrum (Figure 2C) is dominated by the broadband blackbody radiation and shows relatively weak emission features of sodium (Na) and lithium (Li) atoms. The absence of the RMNP oxidation products in the diffusion flame suggests that it is produced solely by the JP-10 oxidation. The weak atomic Na and Li emissions at this stage can be explained if a small amount of the trace alkali metals is extracted into JP-10 after the preparation of the nanofluid.

The lower bounds of the spray droplet sizes are defined by the wavelength of visible light (400–700 nm), as suggested by the white color of the spray observed in optical videos. The upper bound is defined by the resolution of the optical camera which cannot detect individual spray droplets, i.e., 25 μm pixel size. The size range of 0.4–25 μm is consistent with the results of Alexander et al.,³² who observed the breakup of water droplets into a spray of 5–25 μm particles by a carbon dioxide laser at irradiances of 0.2–1 MW cm^{-2} , where higher irradiances produced smaller spray droplets. In our experiment, the peak irradiance of the carbon dioxide laser is about 0.25 MW cm^{-2} . The higher absorption of the carbon dioxide laser light by the nanofluid may additionally stimulate rapid heating of the JP-10 and result in the formation of smaller spray droplets. As suggested by the emission spectrum at 0 ms, spray ignition in

AlNPs starts with JP-10, which may serve as a heat source for AlNPs. In Ti–Al–B RMNPs, no evidence of JP-10 combustion at 0 ms is observed. Instead, the emission spectrum at 0 ms contains only peaks of alkali metal lines, consistent with the internal heating of Ti–Al–B RMNPs. This heating can be explained by exothermic reactions of boron with titanium and aluminum, forming borides which were observed among the oxidation products of Ti–Al–B RMNPs previously.

After ignition, combustion of the nanofluid spray continues in the form of a glow. In the glow flame, JP-10 burns faster in 4–6 ms, and NPs burn for up to 15–20 ms, as suggested by the emission peaks of metal oxides and alkali metals. The latter time is relatively slow for the RMNPs. However, the flames of individual spray droplets in the glow overlap, resulting in the external group spray combustion.³³ In this regime, rates of vaporization and combustion of individual droplets depend on the position in the spray cloud. Thus, the observed decay times for combustion products and the decay of the glow flame may depend on the size and composition of the nanofluid spray cloud. In particular, local equivalence ratios inside the spray cloud can be significantly less than 1, resulting in fuel-rich flames which burn more slowly. Previously, Ti–Al–B RMNP oxidation was studied in an *n*-decane spray flame,²² where nanofluid spray was produced with an atomizer. In that experiment, the spray was burned under stoichiometric conditions, and the analysis of condensed-phase products showed that the RMNPs almost completely burned after 3 ms. This suggests that the equivalence conditions in the nanofluid spray cloud in the current experiment are fuel-rich, resulting in slower combustion.

The glow flame of the nanofluid spray ignites the liquid droplet at 5–10 ms. Sustained plumes attached to the droplets are visible in the optical and IR videos at starting 5 ms after the ignition (Table S1, S2) as bright, hot regions attached to dark/cold spheroid regions. The UV–vis emission spectrum of the liquid droplet flame is dominated by the soot formed under the fuel-rich conditions near the liquid JP-10 surface. The high emissivity of the plumes attached to liquid droplets are supported by IR camera videos consistently showing the highest temperatures of up to 1500 K for these regions. The high emissivity of the blackbody radiation in the diffusion flame can suppress weaker atomic and molecular lines in the emission spectrum because in the high emissivity regime spectral intensities add nonlinearly according to a formula $\epsilon_{\text{tot}} = \epsilon_1 + \epsilon_2 - \epsilon_1\epsilon_2$.³⁴ Here, if $\epsilon_1 \ll 1$ and $\epsilon_2 \approx 1$, the resultant $\epsilon_{\text{tot}} \approx \epsilon_2$, while the spectral contribution from ϵ_1 is multiplied by a factor of $1 - \epsilon_2 \ll 1$. Thus, only the strongest lines with high emissivity or hyperthermal lines can be seen in such a spectrum. However, the absence of strong molecular emissions of AlO and BO₂ and the presence of atomic Na and Li lines in the diffusion flame suggests that the NPs stay trapped inside burning droplets and do not participate in combustion for the time period until the droplet detrap.

Therefore, the combustion of the JP-10 and NPs in the glow flame and the diffusion-limited combustion of liquid droplet constitute two distinct stages of the oxidation of JP-10 droplets doped with Ti–Al–B RMNPs and AlNPs. The main difference between these stages is the nonparticipation of the nanoparticles in the combustion during the second stage. In the current experiments, burning droplets are detrapped in the levitator after about 50 ms without any evidence of NP combustion in the emission spectra. Previously, the combustion of JP-10 droplets doped with Al nanoparticles was studied³⁵ where similarly sized (5 μL) JP-10/AlNP droplets with a much higher AlNP

concentration of up to 40 wt % were suspended on a microfiber and burned for several seconds. In that work, while some of the AlNPs participated in the burning of the liquid droplet, most of the NPs survived until the complete burn-out of JP-10 at about 2 s and burned after that. Therefore, the second stage is detrimental to the practical applications of JP-10 doped with NPs that require a short residence time in the combustion region, such as ramjets,³⁶ and must be avoided by creating conditions that result in the quick and efficient atomization of larger fuel droplets, e.g., via turbulent shear forces to form a nanofluid spray with micrometer-sized droplets that predominantly undergoes glow-type combustion.

In conclusion, the ignition of levitated JP-10 droplets doped with Al nanoparticles (NPs) and Ti–Al–B reactive metal nanoparticles (RMNPs) was studied in the ultrasonic levitator using time-resolved emission spectroscopy by exploiting a newly developed automated deconvolution routine of the UV–vis emission spectra. In both systems, two spatially and temporally distinct stages of combustion were identified for the first time: a glow flame stage, in which small droplets of nanofluid spray quickly combust, and a much slower diffusion flame stage associated with the combustion of larger droplets.

In the glow stage, emission spectroscopy indicates that both the AlNPs and Ti–Al–B RMNPs ignite and oxidize. Furthermore, the time-resolved emission of combustion radicals (CH and C₂) suggests that the glow-stage combustion in JP-10/AlNPs begins via heating provided by the combustion of JP-10. Here, the AlNP oxidation at high temperatures observed in the experiment proceeds in the gas phase via evaporation and gas-phase reactions of aluminum with oxygen. In the JP-10/Ti–Al–B RMNP system, the glow-stage ignition does not involve the organic radicals and JP-10 combustion as a heat source; instead, initial heating could be provided by exothermic titanium and aluminum boride formation. The exoergic intermetallic reactions provide supplemental energy in addition to hydrocarbon combustion and facilitate further metal oxidation reactions. The Ti–Al–B RMNPs' oxidation is multiphase with aluminum evaporation and burning in the gas phase, but Ti and B burning is heterogeneous with the formation of gas-phase products, TiO and BO₂. Additionally, in both systems OH radicals form in reactions of water with metal oxides in the gas phase (BO₂ and AlO) or on the surface (BO). These results show that hydroxyl radicals are a critical contribution to metal oxidation reactions.

The diffusion stages of combustion in both systems start around 5 ms, when the glow flame ignites macroscopic fluid droplets. Under diffusion flame conditions the droplets burn slowly, and the nanoparticles do not participate in combustion at this stage. The nanoparticles engulfed in the JP-10 liquid droplet can survive up to 50 ms of droplet burning before the droplet detraps from the levitator. Thus, the glow flame stage is favorable for metal oxidation and applications where quick combustion and a short residence time are desirable. The rate of combustion in the glow stage may be increased by providing more oxygen to achieve a stoichiometric equivalence ratio. The diffusion stage can be improved in actual combustion systems by providing more efficient atomization of the fluid to form a spray with micrometer-sized droplets that would inherently accelerate droplet combustion.

The findings of this work have far-reaching consequences for designing next-generation propulsion and energy-generating systems. Exploiting the uniquely high volumetric energy density of boron requires understanding intricate heterogeneous

oxidation processes involving boron, oxygen, and hydrocarbon species on a molecular level. Overall, this work presents the first step toward a systematic understanding of distinct combustion stages of multicomponent metal additives to organic fuels such as JP-10. The results demonstrate two distinct stages of burning that will have profound implications on the utilization of high-energy-density nanoparticle additives in liquid jet fuels. The data obtained here will stimulate future studies focused on metal and alloy reaction mechanisms that can impact the first few milliseconds of the combustion process and systematically optimize the nanoparticle/JP-10 ratio critical for better machine designs of next-generation propulsion systems.

■ ASSOCIATED CONTENT

SI Supporting Information

The Supporting Information is available free of charge at <https://pubs.acs.org/doi/10.1021/acs.jpcllett.2c02638>.

Experimental methods; ultrasonic levitator; deconvolution of UV–vis emission spectra; schematic of the levitator system; photograph of the levitator system; pulse sequence diagram; pulse sequence diagram after reference spectra; representative deconvoluted UV–vis spectrum; example of automated deconvolution; spectra and images of JP-10/AlNPs; spectra and images of JP-10/Ti–Al–B RMNPs; peak assignments for JP-10/AlNPs at 0 ms; peak assignments for JP-10/AlNPs at 4 ms; peak assignments for JP-10/AlNPs at 17 ms, JP-10/TiAlB RMNPs at 0 ms, JP-10/TiAlB RMNPs at 2 ms, and JP-10/TiAlB RMNPs at 29 ms (PDF)

Data S1: Base functions from the Pgoopher program. (XLSX)

Movie S1: Levitated droplets ignited by the CO₂ laser (MPG)

Movie S2: Levitated droplets ignited by the CO₂ laser (MPG)

■ AUTHOR INFORMATION

Corresponding Author

Ralf I. Kaiser – Department of Chemistry, University of Hawaii at Manoa, Honolulu, Hawaii 96822, United States; orcid.org/0000-0002-7233-7206; Email: ralfk@hawaii.edu

Authors

Ivan Antonov – Department of Chemistry, University of Hawaii at Manoa, Honolulu, Hawaii 96822, United States

Amandin Chyba – Department of Applied Mathematics and Statistics, Colorado School of Mines, Golden, Colorado 80401, United States

Sahan D. Perera – Department of Chemistry, University of Hawaii at Manoa, Honolulu, Hawaii 96822, United States; orcid.org/0000-0002-4577-9025

Andrew M. Turner – Department of Chemistry, University of Hawaii at Manoa, Honolulu, Hawaii 96822, United States

Michelle L. Pantoya – Mechanical Engineering Department, Texas Tech University, Lubbock, Texas 79409, United States; orcid.org/0000-0003-0299-1832

Matthew T. Finn – U.S. Naval Research Laboratory, Washington, D.C. 20375, United States; orcid.org/0000-0001-9474-7022

Albert Epshteyn – U.S. Naval Research Laboratory, Washington, D.C. 20375, United States; orcid.org/0000-0002-4489-2296

Complete contact information is available at: <https://pubs.acs.org/doi/10.1021/acs.jpcllett.2c02638>

Notes

The authors declare no competing financial interest.

■ ACKNOWLEDGMENTS

The Hawaii group was supported by the United States Office of Naval Research (ONR) under contract number N00014-22-1-2010. M.L.P. is grateful for support from the United States Office of Naval Research (ONR grant number N00014-22-2006 and ONR STEM grant N00014-21-2519). M.T.F. and A.E. are grateful for support from ONR and the NRL base program.

■ REFERENCES

- (1) Davy, H. The Bakerian Lecture, on some new phenomena of chemical changes produced by electricity, particularly the decomposition of the fixed Alkalies, and the exhibition of the new substances which constitute their bases; and on the general nature of alkaline bodies. *Philosophical Transactions of the Royal Society of London* **1808**, 98, 1–44.
- (2) Manuel, P. Computational aspects of carbon and boron nanotubes. *Molecules* **2010**, 15 (12), 8709–8722.
- (3) Tian, Y.; Guo, Z.; Zhang, T.; Lin, H.; Li, Z.; Chen, J.; Deng, S.; Liu, F. Inorganic boron-based nanostructures: Synthesis, optoelectronic properties, and prospective applications. *Nanomaterials* **2019**, 9 (4), 538.
- (4) Majedi, S.; Behmagham, F.; Vakili, M. Theoretical view on interaction between boron nitride nanostructures and some drugs. *Journal of Chemistry Letters* **2020**, 1 (1), 19–24.
- (5) Li, W.-L.; Chen, X.; Jian, T.; Chen, T.-T.; Li, J.; Wang, L.-S. From planar boron clusters to borophenes and metalborophenes. *Nature Reviews Chemistry* **2017**, 1 (10), 0071.
- (6) Yan, Q.-B.; Sheng, X.-L.; Zheng, Q.-R.; Zhang, L.-Z.; Su, G. Family of boron fullerenes: General constructing schemes, electron counting rule, and ab initio calculations. *Phys. Rev. B* **2008**, 78 (20), 201401.
- (7) Xu, S.-G.; Zhao, Y.-J.; Yang, X.-B.; Xu, H. A practical criterion for screening stable boron nanostructures. *J. Phys. Chem. C* **2017**, 121 (21), 11950–11955.
- (8) Singh, B.; Kaur, G.; Singh, P.; Singh, K.; Kumar, B.; Vij, A.; Kumar, M.; Bala, R.; Meena, R.; Singh, A. Nanostructured boron nitride with high water dispersibility for boron neutron capture therapy. *Sci. Rep.* **2016**, 6 (1), 35535. Torresan, V.; Guadagnini, A.; Badocco, D.; Pastore, P.; Muñoz Medina, G. A.; Fernández van Raap, M. B.; Postuma, I.; Bortolussi, S.; Bekić, M.; Čolić, M. Biocompatible iron–boron nanoparticles designed for neutron capture therapy guided by magnetic resonance imaging. *Adv. Healthcare Mater.* **2021**, 10 (6), 2001632.
- (9) Feng, B.; Sugino, O.; Liu, R.-Y.; Zhang, J.; Yukawa, R.; Kawamura, M.; Iimori, T.; Kim, H.; Hasegawa, Y.; Li, H. Dirac fermions in borophene. *Physical review letters* **2017**, 118 (9), 096401.
- (10) Joseph, J.; Sivasankarapillai, V. S.; Nikazar, S.; Shanawaz, M. S.; Rahdar, A.; Lin, H.; Kyzas, G. Z. Borophene and boron fullerene materials in hydrogen storage: opportunities and challenges. *ChemSusChem* **2020**, 13 (15), 3754–3765. Kaur, H.; Kaur, J.; Kumar, R. A review on all boron fullerene (B₄₀): A promising material for sensing and device applications. *Materials Today: Proceedings* **2022**, 48, 1095–1102.
- (11) Epshteyn, A.; Weismiller, M. R.; Huba, Z. J.; Maling, E. L.; Chaimowitz, A. S. Optimization of a High-Energy Ti–Al–B Nanopowder Fuel. *Energy Fuels* **2017**, 31 (2), 1811–1819.
- (12) McCrary, P. D.; Beasley, P. A.; Cojocar, O. A.; Schneider, S.; Hawkins, T. W.; Perez, J. P. L.; McMahan, B. W.; Pfeil, M.; Boatz, J. A.; Anderson, S. L. Hypergolic ionic liquids to mill, suspend, and ignite boron nanoparticles. *Chem. Commun.* **2012**, 48 (36), 4311–4313.

- (13) Connell, T. L., Jr; Yetter, R. A.; Risha, G. A.; Huba, Z. J.; Epshteyn, A.; Fisher, B. T. Enhancement of Solid Fuel Combustion in a Hybrid Rocket Motor Using Amorphous Ti–Al–B Nanopowder Additives. *Journal of Propulsion and Power* **2019**, *35* (3), 662–665.
- (14) Huba, Z. J.; Donakowski, M. D.; Epshteyn, A. Gram-Scale, Low Temperature, Sonochemical Synthesis of Stable Amorphous Ti–B Powders Containing Hydrogen. *Chem. Mater.* **2017**, *29* (4), 1467–1471.
- (15) Weismiller, M. R.; Huba, Z. J.; Maling, E. L.; Epshteyn, A.; Williams, B. A. Air-Stable Nanopowders of Mixed Reactive Metals as Fuel Additives. *MRS Online Proceedings Library* **2015**, *1758* (1), 62–67.
- (16) King, M. K. Boron ignition and combustion in air-augmented rocket afterburners. *Combust. Sci. Technol.* **1972**, *5* (1), 155–164.
- (17) Yeh, C.-L.; Kuo, K. Ignition and combustion of boron particles. *Prog. Energy Combust. Sci.* **1996**, *22* (6), 511–541.
- (18) Epshteyn, A.; Yonke, B. L.; Miller, J. B.; Rivera-Diaz, J. L.; Purdy, A. P. Sonochemically Generated Air-Stable Bimetallic Nanopowders of Group 4 Transition Metals with Aluminum. *Chem. Mater.* **2013**, *25* (6), 818–824.
- (19) Finn, M. T.; Chaloux, B. L.; Epshteyn, A. Exploring the Effects of Reaction Conditions on Morphology and Stability of Sonochemically Generated Ti–Al–B Fuel Powders. *Energy Fuels* **2020**, *34* (9), 11373–11380.
- (20) Brotton, S. J.; Perera, S. D.; Misra, A.; Kleimeier, N. F.; Turner, A. M.; Kaiser, R. I.; Palenik, M.; Finn, M. T.; Epshteyn, A.; Sun, B.-J. Combined Spectroscopic and Computational Investigation on the Oxidation of *exo*-Tetrahydrodicyclopentadiene (JP-10; C₁₀H₁₆) Doped with Titanium–Aluminum–Boron Reactive Metal Nanopowder. *J. Phys. Chem. A* **2022**, *126* (1), 125–144.
- (21) Weismiller, M. R.; Huba, Z. J.; Epshteyn, A.; Fisher, B. T. Combustion of sonochemically-generated Ti–Al–B nanopowders in a premixed methane/air dust flame. *Combust. Flame* **2018**, *191*, 187–194.
- (22) Weismiller, M. R.; Huba, Z. J.; Tuttle, S. G.; Epshteyn, A.; Fisher, B. T. Combustion characteristics of high energy Ti–Al–B nanopowders in a decane spray flame. *Combust. Flame* **2017**, *176*, 361–369.
- (23) Keshavarz, M. H. *Liquid Fuels as Jet Fuels and Propellants: A Review of Their Productions and Applications*; Nova Science Publishers, 2018.
- (24) Brotton, S. J.; Kaiser, R. I. Novel high-temperature and pressure-compatible ultrasonic levitator apparatus coupled to Raman and Fourier transform infrared spectrometers. *Rev. Sci. Instrum.* **2013**, *84* (5), 055114.
- (25) Brotton, S. J.; Kaiser, R. I. In situ Raman spectroscopic study of gypsum (CaSO₄·2H₂O) and epsomite (MgSO₄·7H₂O) dehydration utilizing an ultrasonic levitator. *J. Phys. Chem. Lett.* **2013**, *4* (4), 669–673. Brotton, S. J.; Lucas, M.; Jensen, T. N.; Anderson, S. L.; Kaiser, R. I. Spectroscopic study on the intermediates and reaction rates in the oxidation of levitated droplets of energetic ionic liquids by nitrogen dioxide. *J. Phys. Chem. A* **2018**, *122* (37), 7351–7377. Brotton, S. J.; Malek, M. J.; Anderson, S. L.; Kaiser, R. I. Effects of acetonitrile-assisted ball-milled aluminum nanoparticles on the ignition of acoustically levitated *exo*-tetrahydrodicyclopentadiene (JP-10) droplets. *Chem. Phys. Lett.* **2020**, *754*, 137679. Lucas, M.; Brotton, S. J.; Min, A.; Woodruff, C.; Pantoya, M. L.; Kaiser, R. I. Effects of size and prestressing of aluminum particles on the oxidation of levitated *exo*-tetrahydrodicyclopentadiene droplets. *J. Phys. Chem. A* **2020**, *124* (8), 1489–1507.
- (26) Lucas, M.; Brotton, S. J.; Min, A.; Pantoya, M. L.; Kaiser, R. I. Oxidation of levitated *exo*-tetrahydrodicyclopentadiene droplets doped with aluminum nanoparticles. *J. Phys. Chem. Lett.* **2019**, *10* (19), 5756–5763.
- (27) Saba, M.; Kato, T.; Oguchi, T. Reaction modeling study on the combustion of aluminum in gas phase: The Al+ O₂ and related reactions. *Combust. Flame* **2021**, *225*, 535–550.
- (28) Glumac, N.; Krier, H.; Bazyn, T.; Eyer, R. Temperature measurements of aluminum particles burning in carbon dioxide. *Combustion science and technology* **2005**, *177* (3), 485–511.
- (29) Mangan, T. P.; Douglas, K. M.; Lade, R. E.; Gobrecht, D.; Decin, L.; Plane, J. M. Kinetic Study of the Reactions of AlO with H₂O and H₂; Precursors to Stellar Dust Formation. *ACS Earth and Space Chemistry* **2021**, *5* (12), 3385–3395.
- (30) Kaskan, W.; Mackenzie, J.; Millikan, R. Origin of the Green Bands in the Boron-Oxygen System. *J. Chem. Phys.* **1961**, *34* (2), 570–574.
- (31) Li, S.; Williams, F. Ignition and combustion of boron in wet and dry atmospheres. In *Symposium (International) on Combustion*, 1991; Elsevier: Vol. 23, pp 1147–1154.
- (32) Alexander, D. R.; Armstrong, J. Explosive vaporization of aerosol drops under irradiation by a CO₂ laser beam. *Applied optics* **1987**, *26* (3), 533–538.
- (33) Sirignano, W. A. Fuel droplet vaporization and spray combustion theory. *Prog. Energy Combust. Sci.* **1983**, *9* (4), 291–322.
- (34) De Ris, J. Fire radiation—a review. *Symposium (international) on combustion*; Elsevier, 1979; Vol. 17, pp 1003–1016.
- (35) Chen, B. H.; Liu, J. Z.; Li, H. P.; Yang, W. J.; Cen, K. F. Laser ignition and combustion characteristics of Al/JP-10 nanofluid droplet. *J. Therm. Anal. Calorim.* **2019**, *135* (2), 925–934.
- (36) King, M. K. Ignition and Combustion of Boron Particles and Clouds. *Journal of Spacecraft and Rockets* **1982**, *19* (4), 294–306.

Recommended by ACS

Combined Spectroscopic and Computational Investigation on the Oxidation of *exo*-Tetrahydrodicyclopentadiene (JP-10; C₁₀H₁₆) Doped with Titanium–Aluminum–Boron Rea...

Stephen J. Brotton, Agnes H. H. Chang, *et al.*

DECEMBER 22, 2021
THE JOURNAL OF PHYSICAL CHEMISTRY A

READ 

Effects of Size and Prestressing of Aluminum Particles on the Oxidation of Levitated *exo*-Tetrahydrodicyclopentadiene Droplets

Michael Lucas, Ralf I. Kaiser, *et al.*

FEBRUARY 17, 2020
THE JOURNAL OF PHYSICAL CHEMISTRY A

READ 

In Situ Sol–Gel Synthesis of Unique Silica Structures Using Airborne Assembly: Implications for In-Air Reactive Manufacturing

Connor R. Barker, Andrew D. Ward, *et al.*

AUGUST 17, 2022
ACS APPLIED NANO MATERIALS

READ 

Effect of Oil Properties on the Generation of Nano-Aerosols During Bubble Bursting Through Crude Oil–Dispersant Slicks

Diego F. Muriel, Joseph Katz, *et al.*

NOVEMBER 05, 2021
LANGMUIR

READ 

Get More Suggestions >